Magnetic properties of the $(Mo_{2/3}R_{1/3})_2AlC$ (R=Ho, Dy) i-MAX phases studied by x-ray magnetic circular dichroism and neutron diffraction

Maxime Barbier [1,2,*] Fabrice Wilhelm [2,†] Claire V. Colin [3] Christine Opagiste [3] Elsa Lhotel,[3] Damir Pinek [2]
Youngsoo Kim,[4] Daniel Braithwaite,[4] Eric Ressouche [5] Philippe Ohresser,[6] Edwige Otero [6]
Andrei Rogalev,[2] and Thierry Ouisse[1,‡]

[1]*Université Grenoble Alpes, Centre national de la recherche scientifique (CNRS),*
Grenoble INP, Laboratoire des Matériaux et du Génie Physique (LMGP), F-38000 Grenoble, France
[2]*European Synchrotron Radiation Facility (ESRF), 71 Avenue des Martyrs, CS 40220, 38043 Grenoble Cedex 9, France*
[3]*Université Grenoble Alpes, Centre national de la recherche scientifique (CNRS), Grenoble INP, Institut Néel, F-38000 Grenoble, France*
[4]*Université Grenoble Alpes, Grenoble INP, Commissariat à l'énergie atomique et aux énergies alternatives (CEA), Interdisciplinary Research
Institute of Grenoble (IRIG), Quantum Photonics, Electronics and Engineering Laboratory (PHELIQS), F-38054, Grenoble, France*
[5]*Université Grenoble Alpes, Grenoble INP, Commissariat à l'énergie atomique et aux énergies alternatives (CEA), Interdisciplinary Research
Institute of Grenoble (IRIG)-Modeling and Exploration of Materials Laboratory (MEM), 38000 Grenoble, France*
[6]*Synchrotron-SOLEIL, L'Orme des Merisiers, Saint-Aubin 91192, France*

We report on the magnetic properties of single crystals of Ho- and Dy-based $(Mo_{2/3}R_{1/3})_2AlC$ i-MAX phases. In these nanolamellar compounds, where planes of R and Mo arranged in a skewed triangular lattice are separated by planes of Al and C, geometrical frustration and magnetic exchange interactions lead to complex magnetic properties. Temperature-dependent bulk magnetization, specific heat, and resistivity measurements reveal two magnetic phase transitions in Dy i-MAX (15 and 12 K) and only one in Ho i-MAX (8.5 K). Strong magnetic anisotropy and metamagnetic transitions with a step at $\frac{1}{3}$ of saturation moment along the crystal a axis are observed in field-dependent bulk magnetization curves. X-ray magnetic circular dichroism measurements unveil induced moments on Mo and Al, and a quantitative estimation of the orbital and spin moments of Mo based on magneto-optical sum rules suggests an unusual interaction between the R $4f$ and the Mo $4d$ magnetic moments. Magnetic structures are derived from neutron diffraction measurements, revealing a zero-field incommensurate amplitude modulated order in both compounds, followed by an antiferromagnetic equal-moments structure at lower temperature for Dy i-MAX. The bulk magnetization $\frac{1}{3}$ step is found to be linked to the flip of one R moment out of three within the planes. Detailed phase diagrams for Ho and Dy i-MAX are derived from these measurements.

I. INTRODUCTION

Rare-earth (RE) intermetallic compounds have been widely studied for the wealth of electronic and magnetic properties that they display. The energy scale is usually dominated by the crystal electric field (CEF) and the Ruderman-Kittel-Kasuya-Yosida (RKKY) exchange interaction [1], which is mediated by the conduction electrons and oscillates in space between positive and negative coupling. Frustration of the magnetic moments can arise from the competition between these oscillating couplings [2] and/or from the geometrical configuration of the RE network [3]. The interaction of the aspherical $4f$ orbitals with the CEF results in magnetocrystalline anisotropy, meaning that the magnetic moments are locked into a preferential direction within the lattice. The confluence of RKKY exchange, competing interactions, and the CEF can then induce a complicated magnetic behavior,

including incommensurability and metamagnetism. The magnetic behavior of intermetallic compounds is therefore the result of a delicate balance between many contributions and can evolve dramatically by changing the RE or the surrounding elements [4].

Recently, a family of RE-based compounds with a $(Mo_{2/3}R_{1/3})_2AlC$ stoichiometry were discovered and synthetized as powders [5]. The structure of these compounds is close to that of the broader $M_{n+1}AX_n$ phase family of nanolamellar materials, where M is an early transition metal (TM), A is an element of groups 13 to 16, and X is either C or N. These phases have been extensively studied in the past years for technological purposes [6,7] as well as for their physical properties that can be readily tuned by replacing elements by other elements of the same or of a nearby group [8]. Chemical exfoliation of these MAX phases allows for the isolation of their two-dimensional (2D) counterparts, MXenes [9]. Furthermore, work conducted on a Ce-based MAX phase derivative has shown that 2D RE-based flakes could be obtained by mechanical exfoliation [10]. When RE ions are added to the growth of MAX phases, $\frac{1}{3}$ of M elements

*Corresponding author: maxime.barbier@grenoble-inp.fr

†Corresponding author: wilhelm@esrf.fr

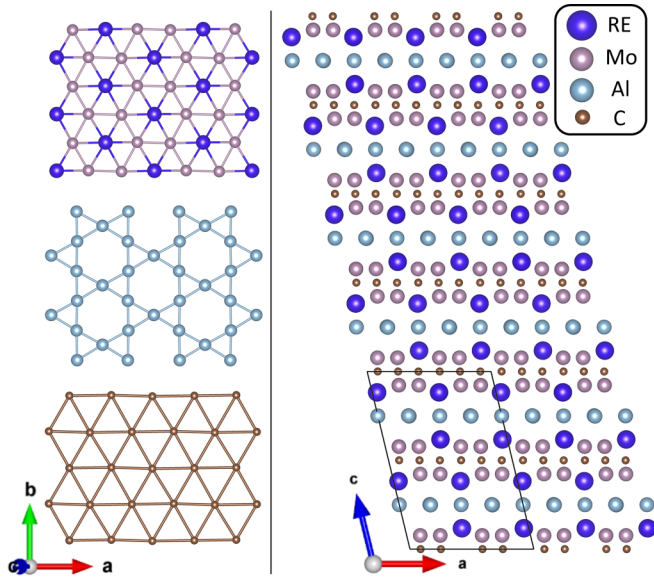‡Corresponding author: thierry.ouisse@grenoble-inp.fr

FIG. 1. Cross-section of the monoclinic crystal structure of $(Mo_{2/3}R_{1/3})_2AlC$ as seen from the a axis (right) and top view of its constituent layers seen from the out-of-plane $c*$ axis (left).

are replaced by RE while keeping the overall MAX phase stoichiometry (here with $M = Mo$, $A = Al$, and $X = C$). This results in alternating planes of Al, C, and Mo/RE where the RE ions order in a skewed triangular lattice that can result in geometric frustration. This, along with the structural anisotropy and the oscillating RKKY couplings of $4f$ magnetic moments through conduction electrons, gives rise to complex magnetic properties. Hereby, we report on the synthesis of single crystals of these RE-based MAX phases, called *i*-MAX phases, where $R = Ho$ and Dy [Fig. 1 shows the monoclinic ($C2/c$) structure, along with a top view of the layers that compose it]. We present bulk measurements, x-ray magnetic circular dichroism (XMCD), and neutron diffraction studies that we have carried out on these single crystals to elucidate magnetic anisotropies and metamagnetism, resolve magnetic structures, and gain insight into the couplings at play in these two compounds.

II. EXPERIMENTAL METHODS

A. Single-crystal growth

The Ho and Dy *i*-MAX single crystals were obtained using the high-temperature solution growth method. RE ingots, Al pellets, and Mo powder were mixed in a sealed graphite crucible and melted in an induction-heated furnace. The typical elemental ratios before C incorporation are around $x_{RE} = 0.7$, $x_{Al} = 0.2$, and $x_{Mo} = 0.1$. Part of the crucible is dissolved into the melt at high temperature, thus supplying the C. The C concentration is mostly dependent on the RE concentration and is estimated to be in the $x_C = 0.2$–0.4 range by weighing the crucible before and after the growth. The temperature is first increased up to 1800 °C within 3 h. The crucible is then slowly cooled down to 1200 °C over 5 to 7 d before turning off the furnace. When it reaches room temperature (RT), the crucible is placed for a few days in an oxidation

chamber through which wet air is flowing. This process is meant to break down the solidified flux into a powder, allowing us to extract the single crystals. The resulting single crystals are rather flat, with an area of a few square millimeters corresponding to the *a-b* crystal planes and a thickness of a few hundred microns in the out-of-plane $c*$ crystal direction. The crystal-growth process is detailed in previous references [11,12]. *i*-MAX single crystals are prone to rotation twinning in the out-of-plane $c*$ direction. To ensure proper crystallinity, transmission Laue diffraction figures were recorded for each crystal used in this paper. As the goal of this paper was to highlight the magnetic anisotropies, we then used a 4-circle diffractometer to find the directions of the a and b crystal axes on selected single crystals. For that purpose, appropriate reflections were chosen, and a pole figure analysis was carried out.

B. Bulk magnetization

For bulk magnetization measurements, we used commercial Quantum Design MPMS magnetometers (Squid VSM and Squid XL), with applied magnetic fields (H) up to 7 T. Quantitative measurements were performed on single crystals of, respectively, 1.92 and 3.17 mg for Ho *i*-MAX and Dy *i*-MAX. To align the applied field along the crystal axes of the single crystals, two different sample holders were used: one for in-plane measurements along the a and b axes and one for the out-of-plane $c*$ direction. Magnetization (M) was recorded as a function of temperature in the 2–300 K temperature range with applied field ranging from 0.01 to 0.1 T, and isothermal magnetization curves $M(H)$ were recorded below and above the magnetic order temperatures of the compounds.

C. X-ray absorption near-edge structure and XMCD

All x-ray absorption measurements were performed on uncleaved, as-grown millimeter-sized crystals. The x-ray absorption near-edge structure (XANES) and XMCD spectra at the $L_{3,2}$ edges of RE and Mo were recorded at the European Synchrotron Radiation Facility (ESRF) ID12 beamline [13]. We exploited the first harmonic of helical undulators of APPLE-II type for RE L edges and of HELIOS-II type for Mo L edges. The spectra were measured using the total fluorescence yield (TFY) detection mode, and the samples were cooled down to $\sim$2.7 K using a He flow cryostat inserted in the bore of a 17 T superconducting magnet. The XANES spectra were corrected for self-absorption effects and were then normalized to match the L-edge statistical ratio: L_3-edge spectra were normalized to unity and L_2-edge spectra to $\frac{1}{2}$. XMCD was then obtained as the direct difference of normalized XANES spectra recorded with right and left circularly polarized x rays. To make sure that the XMCD spectra were free of experimental artifacts, the experiments were performed with an applied magnetic field set both parallel and antiparallel to the incident x rays. Furthermore, XMCD spectra were corrected for incomplete circular polarization rate of the monochromatic x-ray beam ($>$90% at the $L_{3,2}$ edges of RE, $\sim$13% at the Mo L_3 edge, and only $\sim$5% at the Mo L_2 edge). The crystals were mounted in such a way that the angle of the

easy magnetization axis with respect to the applied magnetic field and x-ray propagation direction was 15°.

The XANES and XMCD at the $M_{5,4}$ edges of the RE and the K edge of Al were measured at the DEIMOS beamline at the French synchrotron radiation facility SOLEIL. The cryomagnet of the end-station provides a 7 T magnetic field parallel to the x-ray beam. The spectra were measured using the TFY detection mode, and the samples were cooled down to ~4.3 K. The uncapped Si photodiode is located inside the magnet at 60° with respect to the beam. In this setup, the angle of the easy magnetization axis with respect to the applied magnetic field and x-ray propagation direction was 30°. The beam line, equipment, resolution, and methods are thoroughly described in Refs. [14,15]. The XMCD signals were obtained by reversing the helicity of x rays with fixed direction of the magnetic field. To eliminate experimental artifacts, the XMCD signals were also recorded for reversed direction of the magnetic field. The TFY spectrum at the Al K edge was corrected for self-absorption effects.

D. Heat capacity

Specific heat measurements were conducted using a commercial Quantum Design PPMS on single crystals of 2.09 and 2.12 mg for Dy i-MAX and Ho i-MAX, respectively. The samples were lying flat on the sample holder and held with Apiezon N grease to ensure good thermal conductivity. Because of the growth properties of the single crystals, the out-of-plane c^* axis ends up perpendicular to the surface of the sample holder. A magnetic field up to 2 T was applied in this direction, and measurements were performed in the 2–300 K range.

E. Transport

Resistivity was measured using a Quantum Design PPMS, with temperatures ranging from $T = 2$ to 300 K and a current of 1 mA applied in the a-b plane of Ho i-MAX and Dy i-MAX single crystals.

F. Neutron diffraction

Neutron-diffraction experiments were carried out on the thermal CEA-CRG D23 single-crystal diffractometer at the Institut Laue Langevin (Grenoble, France) with an incident wavelength $\lambda = 1.277$ Å selected by a fixed curvature Cu 200 monochromator. The single crystals used for these measurements were millimeter-sized in the (a,b) plane. For zero-field measurement, the crystals were mounted in a close-cycle refrigerator in 4-circle geometry, and data collections were carried out at several temperatures in the paramagnetic domain and for each of the magnetic phases. The magnetic field diagram was explored in a 6 T vertical field cryomagnet in lifting-counter two-axis geometry. The samples were mounted with the field set along the a crystal axis.

Representational analysis allows the determination of the symmetry-allowed magnetic structures that can result from a second-order magnetic phase transition, given the crystal structure before the transition and the propagation vector of the magnetic ordering. These calculations were carried out using the program SARAh-Representational Analysis [16] and
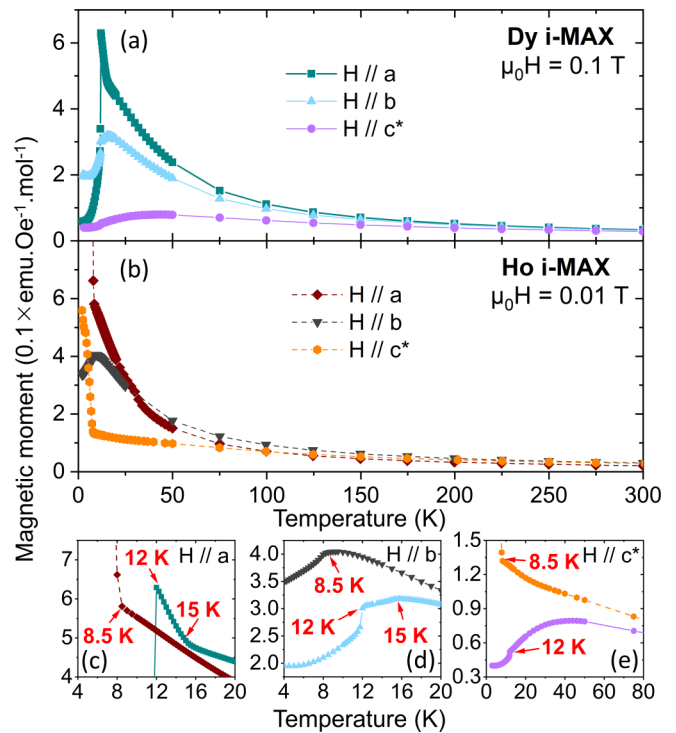
the code BASIREP within the FULLPROF suite [17]. The representational analysis was combined with magnetic space group calculation using ISODISTORT [18] and Bilbao crystallographic server (magnetic symmetry and application software [19]). Crystalline and magnetic structure refinement were performed using FULLPROF [17] for representational analysis formalism and JANA2006 [20] for magnetic space group formalism. To refine the magnetic structures, the crystallographic parameters and the scale factors were fixed to the values obtained in the crystalline refinements. Details on the symmetry analysis are given in the Supplemental Material [21].

III. RESULTS AND DISCUSSION

A. Macroscopic measurements

The temperature and magnetic field dependence of the magnetization was measured along the a, b (in-plane) and c^* (out-of-plane) crystal axes, on Dy- and Ho-based i-MAX single crystals. Figure 2(a) shows the magnetization of Dy i-MAX under a magnetic field of 0.1 T along the three axes (data <30 K are reproduced from Ref. [22]). Above 100 K, $M(T)$ follows a paramagnetic behavior, as confirmed by Curie-Weiss (CW) fittings of the inverse susceptibility, yielding the expected effective moment $\mu_{\text{eff}} = 10.6\,\mu_\text{B}$ for Dy^{3+} (not shown here). A strong anisotropy is observed and could be associated with CEF effects. Along the a axis [Figs. 2(a) and 2(c)], a maximum of $M(T)$ is observed at 15 K, followed by a sharp drop at 12 K, which can be imputed to magnetic

FIG. 2. Bulk magnetization of (a) Dy i-MAX and (b) Ho i-MAX single crystals, measured as a function of T with a small magnetic field ($\mu_0 H = 0.1$ T for Dy i-MAX and $\mu_0 H = 0.01$ T for Ho i-MAX) applied along the a, b, and c^* crystal axes, from 2 to 300 K. (c)–(e) Areas of the magnetic transitions of interest for both compounds, along the three field directions.
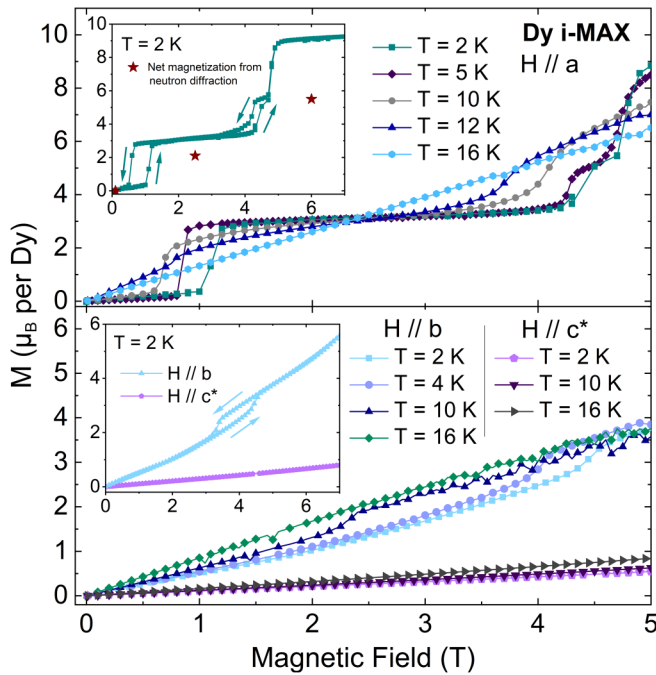
FIG. 3. Isothermal bulk magnetization curves of a Dy *i*-MAX single crystal, measured as a function of applied magnetic field, with *H* aligned along the *a* (top), *b*, and *c** (bottom) crystal axes. The insets show the magnetization curves at $T = 2$ K with increasing and decreasing field up to $\mu_0 H = 7$ T, and all other curves were measured with increasing field only. The arrows differentiate between increasing and decreasing field at the position of the hysteresis. The inset features the net moments determined from neutron diffraction at 2 K.

transitions occurring at these two temperatures. Along the *b* axis [Figs. 2(a) and 2(d)], an initial decline in the slope of $M(T)$ at 15 K is followed by a sharp drop at 12 K. Along the *c** axis [Figs. 2(a) and 2(e)], there is a drop at 12 K and no sign of anomaly at 15 K. However, a broad maximum is observed ∼50 K, resulting in a decrease in the magnetization below that temperature. Such a feature has been observed in RE intermetallics and ascribed to a transition between the ground state CEF level and the first excited state [23,24]. The drops at 12 K along the *a*, *b*, and *c** axes suggest an antiferromagnetic (AFM) order arising below this temperature.

The field dependence of the bulk magnetization is shown in Fig. 3 for temperatures ranging from 2 to 16 K, in units of μ_B per Dy ion (data at 2 K are reproduced from Ref. [22]). The anisotropy is large and highlights the *a* axis as the closest to the easy magnetization axis, as confirmed later in this paper. At 2 K, along the *a* axis, the magnetization increases very slowly at low field, as expected for an AFM state. A first metamagnetic transition takes place at 1 T, leading to a plateau at ∼3.2 μ_B/Dy. A second transition then occurs at 4.5 T, leading to a small plateau at ∼5.5 μ_B/Dy, swiftly followed by a third transition at 5 T, up to a moment of 9.3 μ_B/Dy at 7 T. The XMCD measurements up to 17 T shown in the next section (inset of Fig. 4) display no further transition and a flat profile, suggesting that magnetic saturation has been reached. This value of 9.3 μ_B/Dy should be compared with the expected 10 μ_B/Dy of ionic Dy^{3+}: CEF effects could explain the lower
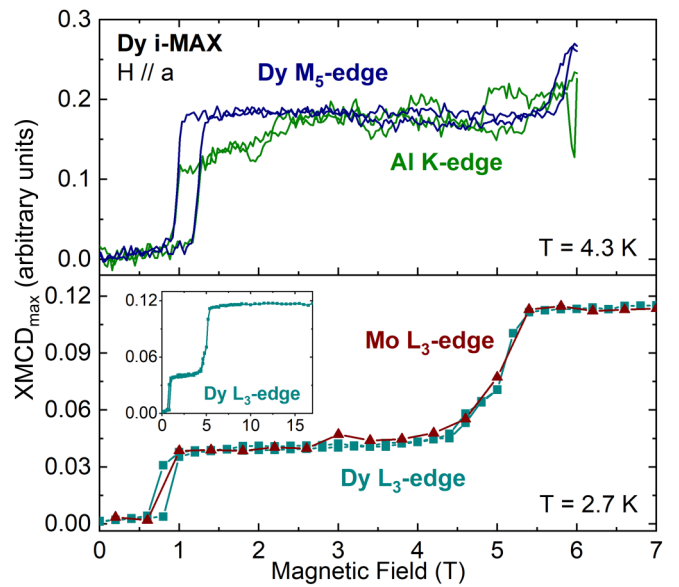

FIG. 4. Dy *i*-MAX element-specific x-ray magnetic circular dichroism (XMCD) intensity vs *H* measured at the Al *K* edge, Dy M_5 edge (top, at $T = 4.3$ K) and Mo/Dy L_3 edge (bottom, at $T = 2.7$ K). The inset at the bottom shows the Dy L_3-edge XMCD intensity up to $\mu_0 H = 17$ T. The divergence between the Al *K* edge and Dy M_5 right after the first transition can be ascribed to measurement artifacts.

moment. It should be noted that the first metamagnetic step reaches ∼$\frac{1}{3}$ of the saturation moment, suggesting an up-up-down configuration of the moments within the *a-b* planes. The transitions at 1 and 4.5 T display a hysteresis, which is characteristic of first-order transitions [25]. The behavior along the easy axis can be compared with the results reported on a hexagonal layered compound, DyAlGa [26]. It also displays an initial AFM-like slope, as well as a hysteretic metamagnetic transition to $\frac{1}{3}$ of the saturation moment. However, for DyAlGa, the uniaxial anisotropy constrains the easy axis to the out-of-plane direction, and the in-plane behavior is fully isotropic. When the temperature increases >2 K, the critical field of the first metamagnetic transition decreases slowly, reaching a minimum at 10 K, and then increases again until it vanishes at 15 K. The positions of the second and third metamagnetic transitions remain stable until 5 K. Between 5 and 10 K, they merge into a single transition that takes place at lower field as the temperature is increased until it vanishes at 15 K.

At 2 K, along the *b* axis, a small metamagnetic step displaying hysteresis occurs at 4.5 T. As *T* increases, the critical field decreases quickly until it vanishes ∼12 K. Studying the ratio of the critical fields along the *a* and *b* axes allows us to conclude that this metamagnetic step along *b* is not merely a projection of the first transition along *a*. The behavior along the out-of-plane *c** direction is linear and does not display any steps.

The magnetic phase transitions of Dy *i*-MAX are summarized in Fig. 5, in the form of *H*-*T* phase diagrams. The data points outlining the domains were extracted from all the measurements displayed in this paper (bulk magnetization, XMCD, specific heat, and neutron scattering). Figure 5(a)
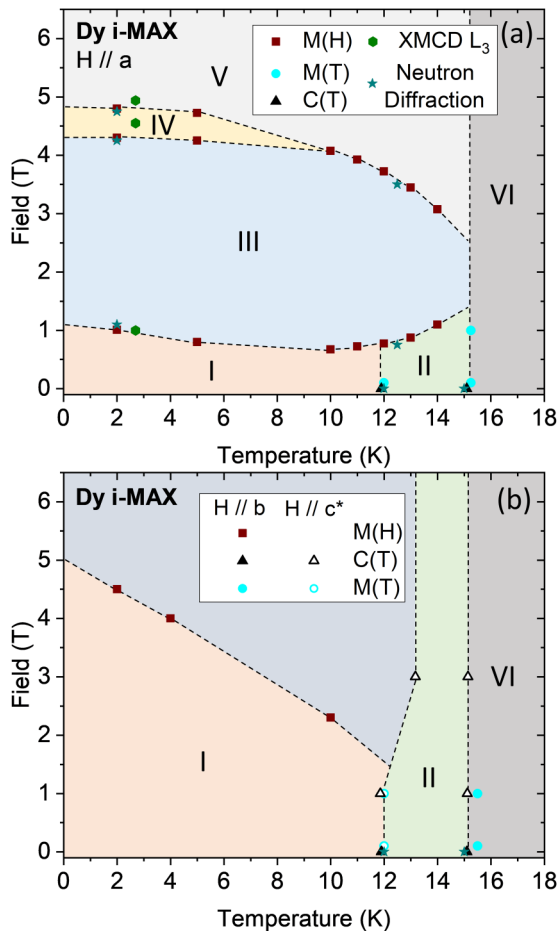
FIG. 5. Magnetic field–temperature phase diagrams derived from all measurements conducted on Dy *i*-MAX, with the field applied (a) along the *a* axis and (b) a combination of axes *b* and *c** (filled symbols for *b* and empty symbols for *c**). The purpose of the dotted lines is to delineate roughly the various areas of the phase diagram, and they should not be taken as the genuine boundaries.

shows the phase diagram with *H* along the *a* axis, where the various areas are labeled from I to VI, and will be discussed further in the section covering neutron diffraction measurements. Figure 5(b) shows the combined phase diagram of *H* along the *b* axis (filled symbols) and the *c** axis (empty symbols). Where there are hysteretic openings, the critical field reported in the phase diagrams is the highest one.

Figure 2(b) shows the magnetization as a function of temperature for Ho *i*-MAX. As for Dy *i*-MAX, there is paramagnetic and anisotropic behavior >100 K, confirmed by the CW fitting that yields the expected $\mu_{\mathrm{eff}} = 10.4\,\mu_B$ for Ho^{3+}. However, a single magnetic transition occurs at 8.5 K and is characterized by a sudden increase in the magnetization along the *a* and *c** axes and a maximum along the *b* axis [Figs. 2(b)–2(e)]. No broad maximum can be seen along *c**, as opposed to Dy *i*-MAX, which can be explained by the shifts in the CEF level scheme that result from changing the RE element.

The Ho *i*-MAX magnetization as a function of applied field at $T = 2$ K is shown in Fig. 6, in units of μ_B per Ho ion. The anisotropy is strong, and like Dy *i*-MAX, the easiest
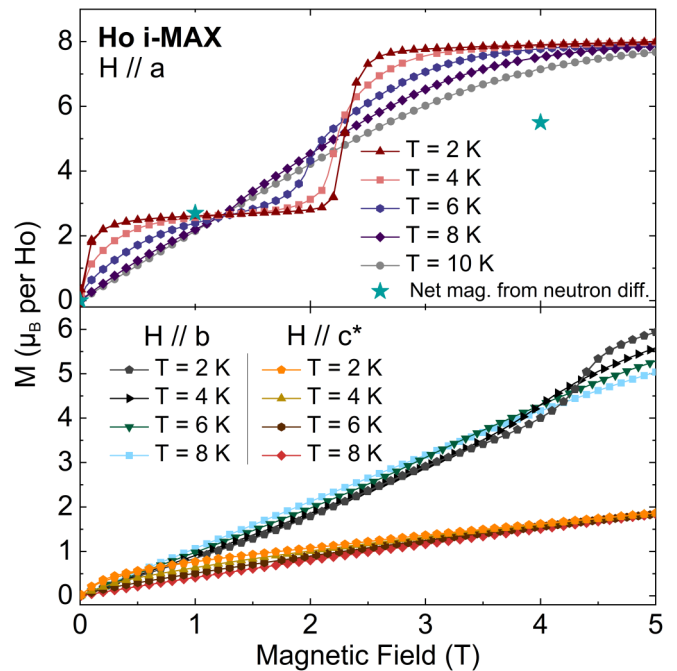

FIG. 6. Isothermal bulk magnetization curves of a Ho *i*-MAX single crystal, measured as a function of applied magnetic field, with *H* aligned along the *a* (top), *b*, and *c** (bottom) crystal axes. The magnetization curves at $T = 2$ K were measured with increasing and decreasing field, while the curves at other temperatures were measured with increasing field only. The net moments determined from neutron diffraction at 2 K are also plotted.

magnetization axis is along *a*, while the hardest one is along *c**. As opposed to Dy *i*-MAX, the magnetization increases very fast at low field, and the first metamagnetic step is quickly reached at ∼2.7 μ_B/Ho. The second transition then occurs >2 T, leading to a moment of ∼8 μ_B/Ho at 7 T. It is worth noting that this saturation moment is much lower than the 10 μ_B expected for Ho^{3+} ions, while it is much closer to the expected ionic value in Dy *i*-MAX. This observation was also made in the *R*AlGa family, where the DyAlGa mentioned earlier [26] saturates at 9.67 μ_B/Dy, while the HoAlGa saturation moment is limited to 8.06 μ_B/Ho [27]. This difference could be explained both by CEF effects and the angle between the *a* axis and the easy magnetization axis, as supported by the neutron diffraction measurements presented below. Moreover, it has been shown that the value of the *i*-MAX magnetic moments keeps increasing as *T* decreases below the magnetic order temperature, which was ascribed to magnetic fluctuations [28]. It is therefore likely that bulk magnetization measurements at a $T < 2$ K would yield a saturation moment closer to the expected value. No hysteresis is observed in the transitions, and there is no sign of an intermediate step between the $\frac{1}{3}$ plateau and saturation, as opposed to Dy *i*-MAX. However, the first metamagnetic step is also set at $\frac{1}{3}$ of the saturation moment. The isothermal $M(H)$ curves were measured at different temperatures between 2 and 10 K (Fig. 6). The critical field of the metamagnetic transition initially decreases quite slowly, before decreasing faster ∼5 K up until it drops down to zero at 8.5 K.
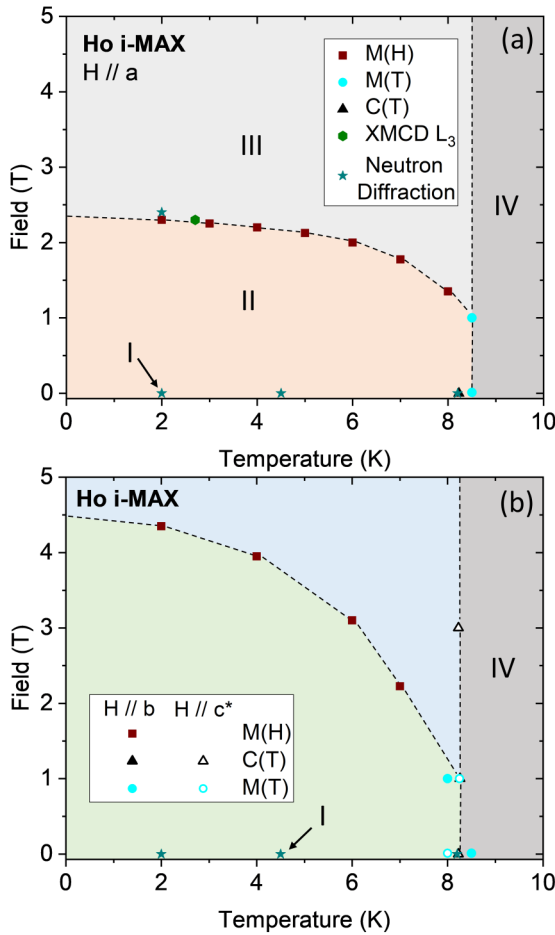
FIG. 7. Magnetic field–temperature phase diagrams derived from all measurements conducted on Ho *i*-MAX, with the field applied (a) along the *a* axis and (b) a combination of axes *b* and *c** (filled symbols for *b* and empty symbols for *c**). The phase labeled I corresponds to the zero-field magnetic order.

Along the *b* axis, the $M(H)$ curve is linear up to 4 T, where a smooth metamagnetic transition leads to a moment of 6 μ_B/Ho at 5 T. Along *c**, there is a curvature at low field, followed by a linear magnetization up to 5 T.

The *H-T* phase diagrams for Ho *i*-MAX are displayed on Fig. 7, where (a) shows the phase diagram with *H* along the *a* axis, and (b) shows the combined phase diagrams of *H* along the *b* axis (filled symbols) and the *c** axis (empty symbols). Here, phase I refers to the zero-field magnetic order, which vanishes as soon as a field is applied (cf. neutron diffraction section), hence the arrow pointing at the *x* axis.

Heat capacity and resistivity measurements as a function of temperature are shown in Fig. 8. The resistivity as a function of temperature up to 300 K shows a metallic behavior for the two phases [Figs. 8(a) and 8(b)]. For Dy *i*-MAX, the transition at 15 K results in an upturn in the resistivity, followed by a drop at the second transition at 12 K. For Ho *i*-MAX, the transition at 8.5 K also causes an upturn in the resistivity, which suggests similarities with the first Dy *i*-MAX transition and is discussed further in the section dedicated to neutron diffraction. There is a small anomaly of unknown origin at ~40 K in the resistivity of Ho *i*-MAX.
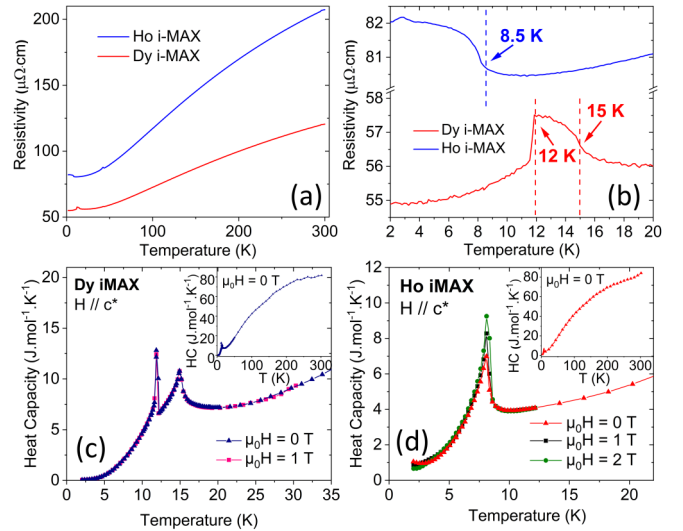

FIG. 8. (a) Transport measurements on Ho and Dy *i*-MAX single crystals, as a function of temperature, with (b) the region of the magnetic transitions. Heat capacity as a function of temperature for (c) Dy *i*-MAX and (d) Ho *i*-MAX, with and without applied magnetic field. The insets show the full temperature range.

For Dy *i*-MAX, there are two λ anomalies at 15 and 12 K in the heat capacity [Fig. 8(c)], which can be ascribed to the two magnetic phase transitions observed on the $M(T)$ data of Fig. 2. When a field of 1 T is applied in the out-of-plane *c** direction, the shape of the anomalies is unchanged. For Ho *i*-MAX, a single λ anomaly is observed at 8.5 K, corresponding to the transition to the magnetic order [Fig. 8(d)]. However, applying a magnetic field seems to decrease the heat capacity jump amplitude. It is worth mentioning that, at 300 K [insets of Figs. 8(c) and 8(d)], the heat capacity reaches 82 J mol^{-1} K^{-1} for Dy *i*-MAX and 83 J mol^{-1} K^{-1} for Ho *i*-MAX. This is below the $3NR \approx 100$ J mol^{-1} K^{-1} expected for these compounds, where N is the number of atoms in a formula unit, and R is the gas constant. A neutron and density functional theory (DFT) study of the phonon modes of Cr_2AlC, another MAX phase with similar stoichiometry, showed that part of the acoustic modes and all the optic modes involving C are not excited yet at 300 K [29]. *I*-MAX phases contain heavier elements that lower the excitation energies of the acoustic modes, but it is plausible to assume that the C optic modes are not activated either at 300 K, explaining the difference between the expected heat capacity and the measured values.

B. XMCD

The local microscopic magnetic properties of the Ho and Dy *i*-MAX phases were then studied with XMCD. This spectroscopic method yields a shell-specific measure of the magnetism of the probed element. Indeed, since the binding energy of the absorption edges is unique to each chemical element, their electronic and magnetic properties can be probed independently within a compound. Figure 9 shows the XANES and XMCD spectra measured at the Dy and Ho $L_{3,2}$ edges of Dy *i*-MAX and Ho *i*-MAX, with a magnetic field applied close to the *a* axis. At the $L_{3,2}$ edges of RE, the
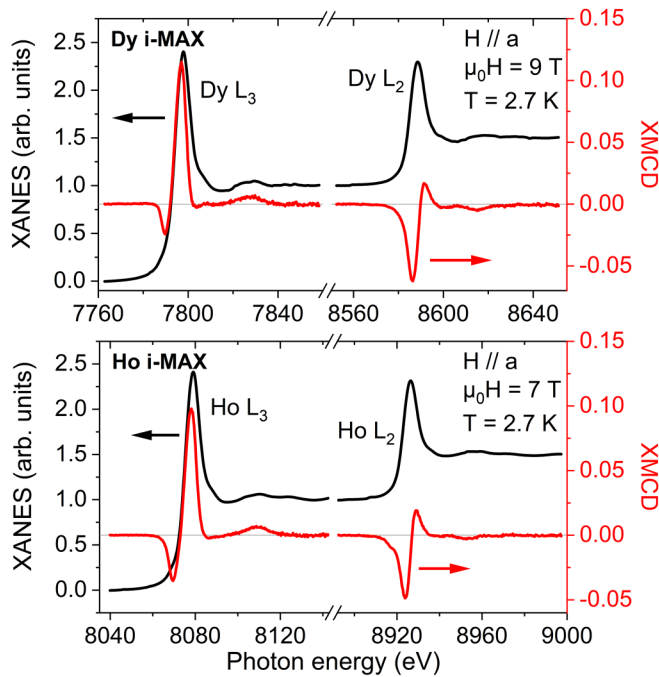
FIG. 9. Normalized $L_{3,2}$-edge x-ray absorption near-edge structure (XANES; left axis) and x-ray magnetic circular dichroism (XMCD; right axis, same scale as XANES) spectra measured at $T = 2.7$ K on Dy i-MAX (top) and Ho i-MAX (bottom), with a magnetic field applied close to the a axis.
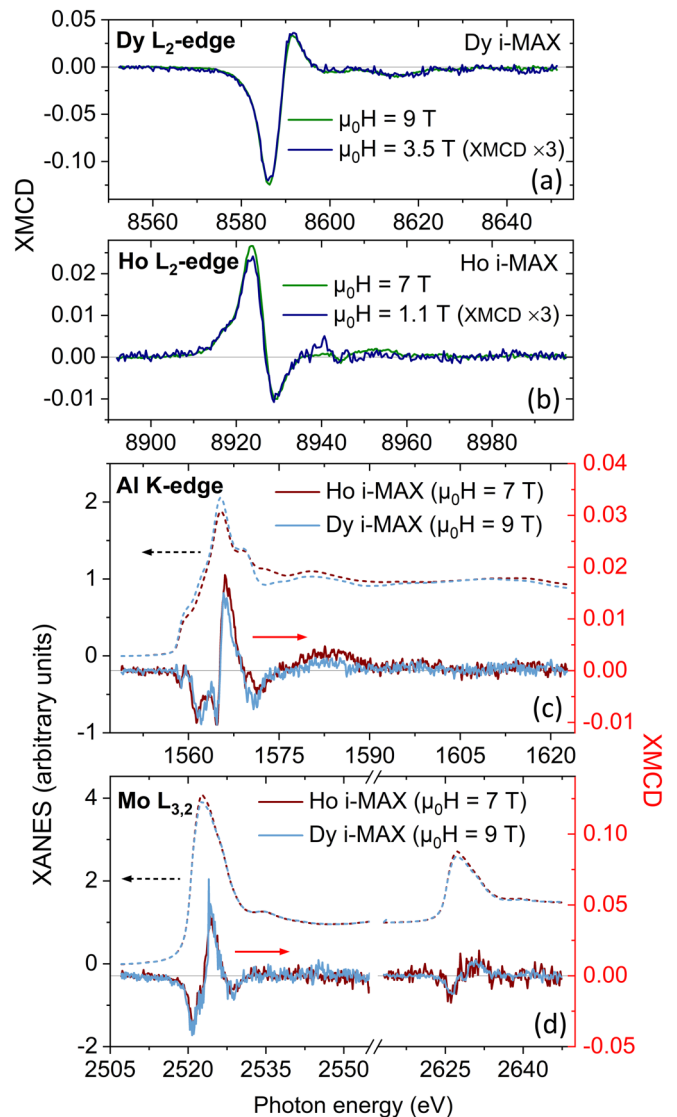

FIG. 10. X-ray magnetic circular dichroism (XMCD) spectra at the L_2 edges of (a) Dy and (b) Ho, with applied fields allowing us to reach the first metamagnetic step as well as saturation. The spectrum at the first step is multiplied by a factor of 3 for comparison purposes. X-ray absorption near-edge structure (XANES)/XMCD at (c) the K edge of Al and (d) $L_{3,2}$ edges of Mo, on Ho and Dy i-MAX, at saturation field. For all measurements, the field is applied close to the a axis.

absorption is mainly due to dipolar transitions ($2p$ electrons excited to the $5d$ shell), with a smaller quadrupolar contribution ($2p$ to $4f$). The magnitude of the applied field is of 9 T for Dy i-MAX and 7 T for Ho i-MAX. Those fields allow us to reach the last magnetization steps of Figs. 3 and 6 and therefore to approach saturation. The L_3-edge XMCD signal features a first negative peak followed by a more intense positive peak that can be assigned to the quadrupolar and dipolar contributions, respectively [30]. The dipolar peak reaches 12% of the XANES edge jump for Dy i-MAX and 10% for Ho i-MAX. These values are in fair agreement with amplitudes of XMCD signals observed close to magnetic saturation of heavy RE atoms [31,32]. Unfortunately, it is not possible to extract more quantitative information from the XMCD spectra at the $L_{3,2}$ edges of RE [33].

Figures 10(a) and 10(b) display RE L_2 XMCD spectra recorded on the metamagnetic $\frac{1}{3}$ step ($\mu_0 H = 3.5$ T for Dy i-MAX and $\mu_0 H = 1.1$ T for Ho i-MAX) as well as at saturation field ($\mu_0 H = 9$ T for Dy and $\mu_0 H = 7$ T for Ho). The XMCD signal at the step has the same spectral shape and the same amplitude as the one at saturation when the former is multiplied by a factor of 3, as in macroscopic measurements. This observation suggests that, in these crystals, the magnetic properties are driven by the magnetism of RE ions.

To assess the involvement of Al and Mo in the magnetism of these i-MAX compounds, we have performed XMCD measurements at the K edge of Al (mostly $1s$-to-$3p$ transitions) and at the $L_{3,2}$ edges of Mo (mostly $2p$-to-$4d$ transitions). The spectra obtained at saturation field for Ho and Dy i-MAX are shown in Figs. 10(c) and 10(d). At the K edge of Al,

the XANES spectrum measured on Ho i-MAX displays an additional feature at 1573 eV with respect to the spectrum recorded on Dy i-MAX. This likely arises from a thicker Al oxide surface layer in Ho i-MAX crystal than the Dy i-MAX sample. This hypothesis is supported by total electron yield measurements (not shown) that are more surface sensitive. The Al K-edge XMCD spectra shown in Fig. 10(c) display a sizeable signal on both compounds, revealing a finite magnetic polarization of the Al $3p$ states. The XMCD spectral shape and amplitude are very similar for the two compounds, despite the differences observed in the XANES spectra.

The XANES spectra recorded at the $L_{3,2}$ edges of Mo for Dy and Ho i-MAX crystals are reproduced in Fig. 10(d).

TABLE I. Mo $4d$ orbital and spin magnetic moments derived by means of the magneto-optical sum rules, for Ho and Dy i-MAX. The error bars are estimated to be of the order of 10% of the values.

i-MAX phase	Mo spin moment m_s (μ_B/Mo)	Mo orbital moment m_l (μ_B/Mo)
Ho i-MAX	7×10^{-3}	4×10^{-3}
Dy i-MAX	9×10^{-3}	5×10^{-3}

The spectra are dominated by strong resonances (white lines) corresponding to transitions from the core $2p$ states to empty $4d$ states of Mo. A small difference in white line intensity between the two compounds indicates that the number of Mo $4d$ electrons is slightly higher in Dy i-MAX. The $L_{3,2}$ XMCD spectra display a sizeable signal, which clearly indicates that Mo $4d$ states are magnetically polarized and carry a magnetic moment. In Mo$_4$Ce$_4$Al$_7$C$_3$, a related compound with similar RE/Mo layers, no polarization was observed at the $L_{3,2}$ edges of Mo [34]. Application of the magneto-optical sum rules [35,36] allows us to extract quantitative values for these moments and disentangle their orbital and spin contributions. Details on the sum rules and their use in the present case are given in the Supplemental Material [21] (see also Refs. [37,38] therein). The Mo $4d$ magnetic moments thus determined are given in Table I. For both compounds, the values of the spin and orbital moments are found to be 2 to 3 orders of magnitude smaller than those measured in the bulk magnetization. This means that the vast majority of the magnetic moment is carried by the RE and justifies the normalization of the bulk magnetization to μ_B per RE atom (Figs. 3 and 6). Such small moments cannot result from an intrinsic Mo $4d$ moment. For instance, in MoCu$_2$-Meen, a molecular compound featuring photoinduced paramagnetism with an intrinsic magnetic moment carried by Mo, the total magnetic moment reaches 1.35 μ_B, as determined with the sum rules [39]. Instead, they must be of induced nature and arising from hybridization of the Mo $4d$ with the $5d$-$4f$ orbitals of the RE atoms. This is akin to what is observed in Co$_{96}$Mo$_4$, an alloy where the Mo magnetic moment is also induced by its proximity with the strongly magnetic Co atoms [40].

The sum rules give us an opportunity to study the magnetic interactions at play in these compounds. The positive values of the Mo $4d$ moments indicate that both the spin and orbital components are parallel to the applied magnetic field and therefore to the $4f$ moment of RE. The parallel alignment of the spin and orbital moments unveils an unusual coupling scheme between the RE and the Mo moments. Indeed, in intermetallic compounds, it is generally admitted that the coupling between the RE $4f$ and TM nd shells is mediated by the RE $5d$ shell since the RE $4f$ is too localized and screened to have any meaningful direct interaction with the TM nd shell. In this scheme, the internal RE $4f$-RE $5d$ exchange coupling results in an induced $5d$ spin that is parallel to the $4f$ spin [41]. Then the coupling of the TM nd and RE $5d$ spins follows the rules of the d-d coupling of TM binaries: It is parallel if both elements belong to the same half of the series and antiparallel if they do not [42]. Here, the RE is at the beginning of the transition series since the number of $5d$ electrons is small for all RE elements. As for the orbital moments, their direction is usually governed by Hund's rules. For example, in the case

of the Co$_{96}$Mo$_4$ alloy mentioned above, the spin and orbital moments induced on the Mo were found to be antiparallel [40], which agrees with Hund's third rule since the Mo $4d$ shell is less than half-filled. Surprisingly, this scheme breaks down in the case of Ho and Dy i-MAX, where the Mo $4d$ orbital and spin moments are parallel to each other. Such a breaking of Hund's third rule in a solid-state system has, for instance, been observed in the case of induced moments in W and Zr [43,44]. A plausible interpretation for this could be related to a direct interaction between the RE $4f$ spin and orbital moments and the Mo $4d$ spin and orbital moments, as opposed to the indirect $4f$-$5d$-$4d$ interaction covered above.

The XMCD technique allows us to record so-called element-specific magnetization curves, by monitoring the intensity of the XMCD signal at fixed energy as a function of applied magnetic field. These measurements were conducted at the Al K edge, Mo L_3 edge, and RE L_3 and M_5 edges and are displayed in Figs. 4 and 11, respectively, for Dy and Ho i-MAX. The measurements at the RE M_5 edge and Al K edge were conducted at the DEIMOS beamline and are displayed separately from those at the RE and Mo L_3 edge that were carried out at ESRF ID12. The metamagnetic transitions occur at different critical fields on the two batches of measurements, which can be explained by the different angles between applied field and the easy magnetization axis of the
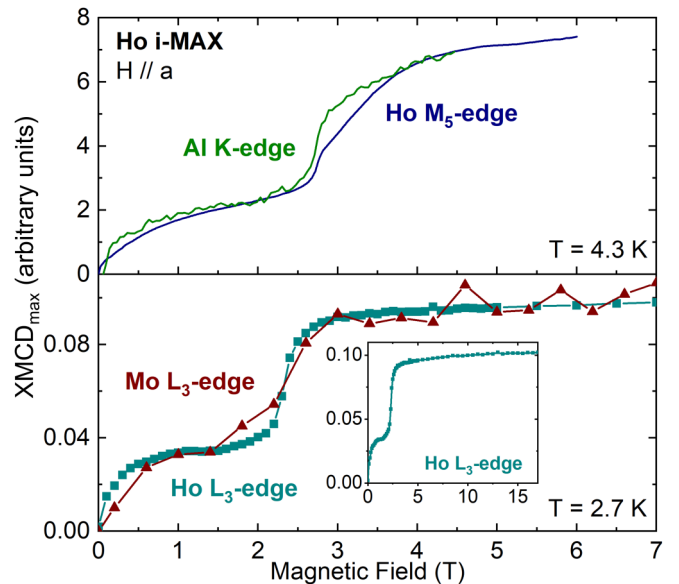

FIG. 11. Ho i-MAX element-specific x-ray magnetic circular dichroism (XMCD) intensity vs H measured at the Al K edge, Ho M_5 edge (top, at $T = 4.3$ K), and Mo/Ho L_3 edge (bottom, at $T = 2.7$ K). The inset at the bottom shows the Ho L_3-edge XMCD intensity up to $\mu_0 H = 17$ T.

sample on the two experimental setups, as described in the methods section. It is obvious from Fig. 4 that the Dy magnetization recorded at the L_3 and M_5 edges is following the bulk magnetization shown in Fig. 3: The first metamagnetic step and the hysteretic opening are reproduced, as well as the transition to the saturation state at L_3 (the field was not intense enough to reach saturation at M_5). Moreover, the Mo L_3-edge and Al K-edge magnetization is in turn following closely that of Dy L_3 and M_5. To maximize the signal-to-noise ratio, the measurements on Mo were averaged over the field up and down loop, which explains why no hysteresis can be seen in the Mo L_3 XMCD$_{max}(H)$ curve. However, since the behavior is otherwise closely following that of Dy, the Mo L_3 should also display that hysteresis. The element-specific magnetization curve measured on Ho i-MAX shows the same behavior, with the RE, Al, and Mo following the bulk magnetization, as shown in Fig. 11. This is further proof that the magnetic moments of the Mo $4d$ and Al $3p$ orbitals are induced and that the magnetic properties of these compounds are dominated by the RE magnetic behavior.

C. Neutron diffraction

To uncover the magnetic structures of Ho and Dy i-MAX at the various areas of their phase diagrams, this paper was complemented with a neutron diffraction study. Measurements were conducted as a function of temperature and magnetic field, with H applied along the easy magnetization a axis. The data analysis was conducted under the assumption that the magnetic moments are only carried by the RE elements and that the other elements of the compounds do not take part in the magnetic structure. This assumption is justified by the XMCD study conducted at the $L_{3,2}$ edges of Mo, which shows that the Mo atoms carry an induced moment $<0.01\ \mu_B$. It is fair to assume that Al and C do not carry a significant magnetic moment either.

The symmetry analysis is described in the Supplemental Material [21] (see also Refs. [45,46] therein), along with details regarding the determination of the magnetic structures at each point in temperature and applied magnetic field for Ho and Dy i-MAX. Graphical representations of the quality of the refinements are also provided.

1. Dy i-MAX

The structural refinement of Dy i-MAX (see Table S3 in the Supplemental Material [21]) based on single-crystal neutron diffraction data at 80 K confirmed the structural model previously reported, based on powder x-ray diffraction [5]. The refinement quality is rather poor, which is most likely due to the small size of the single crystal used for this paper.

First, the reciprocal space was explored at zero field and as a function of T (see Figs. S1(a) and S1(b) in the Supplemental Material [21]) to identify the propagation vectors involved. The first phase transition at 15 K leads to an AFM incommensurate magnetic structure, with a propagation vector $k_{inc} = (0, k_y, 0)$ with $k_y = 0.605(5)$, which corresponds to phase II of the phase diagram in Fig. 5. Then when T decreases further, there is a second transition ~ 12 K leading to a commensurate structure, with a propagation vector $k_{1/2} = (0, \frac{1}{2}, 0)$ which remains down to 2 K and corresponds

to phase I in Fig. 5. This behavior is in line with what was observed in the bulk magnetization, specific heat, and resistivity as a function of temperature, where the two transitions are clearly visible. This transition to an incommensurate order followed by a transition to commensurability at lower temperature is commonly observed in RE-based compounds and is explained in two ways in the literature. In the first picture, the oscillatory and long-range RKKY exchange interactions produce interionic couplings that are competing and cannot be satisfied at the same time, which leads to a magnetic order that is not commensurate with the lattice. The transition to a commensurate order is then the result of an interplay between exchange interactions and CEF anisotropy, which favors large and equal magnetic moments at 0 K [1,2,47]. In the second picture, the incommensurate order could be explained by the onset of a spin density wave (SDW), which could be due to a Fermi surface instability caused by nesting and is quite common in low-dimensional materials [48–50]. An extensive angle-resolved photoemission spectroscopy (ARPES) study would be required to prove this hypothesis. The nesting effect can be estimated by computing the Lindhard response function from the band structure [51]. The transition to the incommensurate order is identified by an abrupt upturn in the resistivity [Fig. 8(b)]. This has been observed in many compounds displaying a transition to a SDW and has been ascribed to the emergence of an energy gap in the Fermi surface due to the onset of the SDW [52–55]. However, it is worth mentioning that, in other compounds, this transition to a SDW is characterized by a drop in the resistivity, instead of an upturn [56,57].

To determine the zero-field magnetic structure of these two phases, we then collected data at 12.5 and 2 K. Representations of these structures are shown in Fig. 12.

At $T = 2$ K and $\mu_0 H = 0$ T, the magnetic phase is commensurate with a k vector equal to $\frac{1}{2}$ along b. The best magnetic model is a collinear AFM structure with the magnetic moment aligned along the a axis (detailed description in Table S4 in the Supplemental Material [21]). The refinement of components along b and c does not significantly improve the fit, and the refined ordered magnetic moment is only $5.6(1)\ \mu_B$/Dy, which is small in comparison with the value expected of Dy ions. This zero-field and low-T magnetic arrangement is like the one derived from neutron powder diffraction [22], the only difference being the absence of the small c-axis component.

At $T = 12.5$ K and $\mu_0 H = 0$ T, the magnetic phase is incommensurate with a propagation vector $k_{inc} = (0, 0.605, 0)$. Here, the analysis is made difficult by the small intensity of the observed magnetic signal, leading to poor refinement quality. The magnetic structure associated with this phase is an amplitude modulated transverse magnetic structure with magnetic moments aligned along a, as displayed in Fig. 12. The modulated moments are forced along a given crystal direction, which is a testament of the strength of the uniaxial crystal field anisotropy: For weaker or planar anisotropy, the incommensurate order is usually helimagnetic for intermetallic compounds [58].

The magnetic field phase diagram was then explored by performing scans along the b direction at 2 K up to 6 T (see Fig. S1(c) in the Supplemental Material [21]). First, a
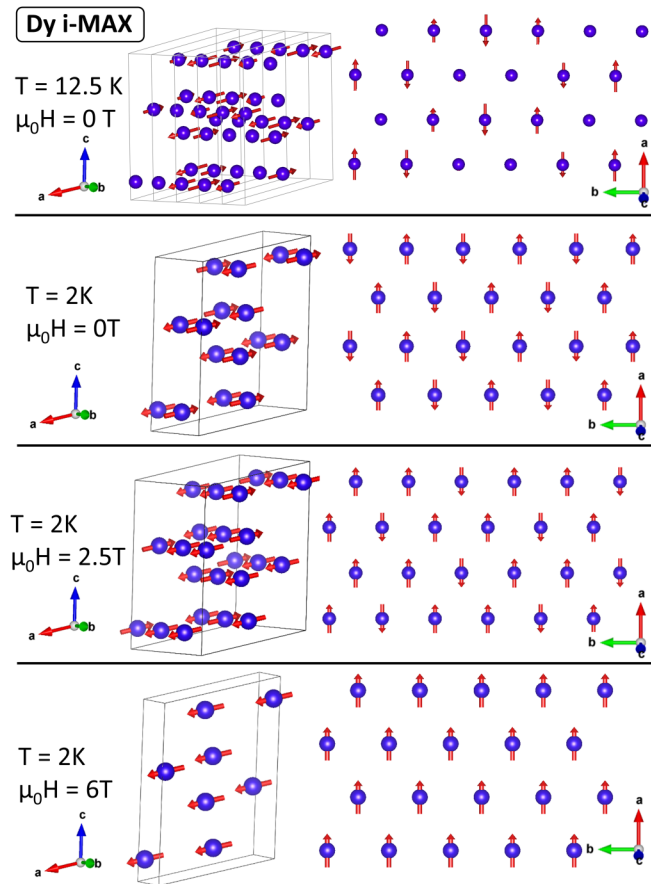
FIG. 12. Dy *i*-MAX magnetic structures determined from neutron scattering measurements conducted with H applied along the *a* axis. The incommensurate phase ($T = 12.5$ K and $\mu_0 H = 0$ T) is followed by the structures at $T = 2.4$ K with applied fields of 0, 2.5, and 6 T ($T = 2.4$ K), corresponding to the ground state, first metamagnetic step, and at saturation. The depiction on the left corresponds to the magnetic unit cell for commensurate phases, and the one on the right pictures a rare-earth (RE) plane as seen from the out-of-plane $c*$ direction. For clarity, only Dy atoms are shown.

clear magnetic transition is observed at 1 T with a change of propagation vector from $k_{1/2}$ (phase I of the phase diagram in Fig. 5) to $k_{2/3} = (0, \frac{2}{3}, 0)$ (phase III). This magnetic signal at $k_{2/3}$ is associated with an additional magnetic signal at $k_0 = (0, 0, 0)$, corresponding to a ferromagnetic (FM) contribution. Then, at 4.3 T, the magnetic signal vanishes at $k_{2/3}$, and the propagation vector becomes incommensurate $k_{inc} = (0, 0.47, 0)$, corresponding to phase IV. Finally, >4.9 T, there is no more magnetic contribution of the form $(0, k_y, 0)$, leaving only $k_0 = (0, 0, 0)$: Saturation is reached, which corresponds to phase V in Fig. 5.

We determined the magnetic structures at two field positions at 2 K: 2.5 and 6 T, corresponding to the first metamagnetic step as well as magnetic saturation (Fig. 12).

At $T = 2$ K and $\mu_0 H = 2.5$ T, as inferred from the bulk magnetization data, an up-up-down ferrimagnetic model gives a satisfactory refinement of the data (see Table S5 in the Supplemental Material [21]). The moments remain aligned along *a*, but one moment out of three flips, yielding an average

moment of $\frac{1}{3}$ of the saturation moment. Each Dy^{3+} ion carries a magnetic moment of 6.3(3) μ_B/Dy, corresponding to a net magnetization of 2.1(1) μ_B/Dy. This is far below the $\sim 3 \mu_B$ measured in the bulk magnetization, which could be explained by the rather poor quality of the data.

The second data collection was then conducted at $T = 2$ K and $\mu_0 H = 6$ T to reach saturation. The magnetic intensities at $k_0 = (0, 0, 0)$ were extracted by subtraction with purely nuclear reflections, and the dataset is rather noisy with a large dispersion of equivalent reflections. The magnetic structure is FM with the moments aligned along the *a* axis (Fig. 12). The ordered magnetic moment is determined to be 5.5(2) μ_B/Dy, which is also far below the $\sim 9 \mu_B$ of the bulk magnetization. It is important to note that, while the values of the moments determined by neutron diffraction are significantly smaller, the behavior remains consistent with bulk magnetization measurements. The moments carried by the individual Dy^{3+} ions remain mostly equal at 0, 2.5, and 6 T, and the up-up-down magnetic structure explains the $\frac{1}{3}$ step observed in Fig. 6. It appears that there is a scaling factor between the neutron moment and the actual moment, which could be explained by the poor quality of the neutron diffraction data.

No data collection was conducted at the position of the incommensurate phase IV. As for the phase labeled VI, it corresponds to the paramagnetic state.

2. Ho i-MAX

The structural refinement based on single-crystal neutron diffraction data (see Table S7 in the Supplemental Material [21]) confirmed that Ho *i*-MAX crystallizes with $C2/c$ symmetry, in good agreement with previous results based on powder x-ray diffraction data [5].

The exploration of the reciprocal space in temperature shows that the magnetic phase stabilized at zero field (phase I in Fig. 7) orders below $T_N = 8.3(3)$ K with a propagation vector $k_y = (0, 0.677, 0)$ independent of temperature (Fig. S5(a) in the Supplemental Material [21]). The behavior in T matches with the bulk magnetization, specific heat, and resistivity as a function of temperature, where only one transition is visible, as opposed to Dy *i*-MAX. This is puzzling because, as mentioned above and explained in detail in Ref. [47], the interplay of the CEF and exchange interactions usually favors equal moments and commensurate magnetic structures at low temperature. However, if the CEF ground state is nonmagnetic, the modulated structure can remain stable down to 0 K [59]. Indeed, Ho^{3+} is non-Kramers, which means that the CEF can split the ground state into nondegenerate and nonmagnetic states, as can, for instance, be observed in $PrNi_2Si_2$ [60]. This is not the case for Dy^{3+}, where the ground state is restricted to magnetic doublets. Uncovering the CEF scheme of Ho *i*-MAX would have allowed us to determine if a transition to commensurability can be expected at lower T, but such a study is made difficult by its low symmetry. As for Dy *i*-MAX, the transition to the incommensurate order is accompanied by an upturn in the resistivity [Fig. 8(b)].

To determine the zero-field magnetic structure, labeled I in Fig. 7, measurements were conducted at 4.5 and 2 K.

At $T = 2$ K and $\mu_0 H = 0$ T, the magnetic phase is incommensurate with a k vector $k_y = (0, 0.677, 0)$ (see Table S2 in
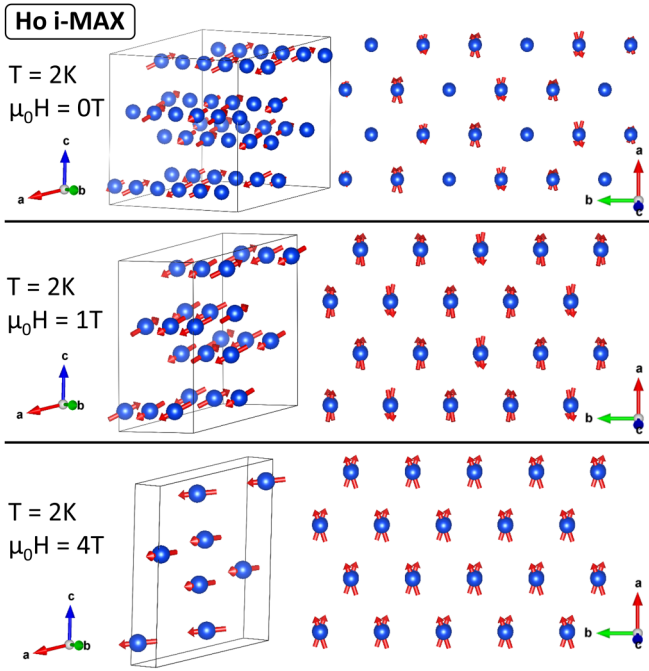
FIG. 13. Ho *i*-MAX magnetic structures determined from neutron scattering measurements conducted with H applied along the a axis. Measurements were done at $T = 2.4$ K with applied fields of 0, 1, and 4 T ($T = 2.4$ K), corresponding to the ground state, metamagnetic step, and at saturation. The depiction on the left corresponds to the magnetic unit cell for commensurate phases. The one on the right pictures two consecutive rare-earth (RE) planes as seen from the out-of-plane c^* direction. For clarity, only Ho atoms are shown.

the Supplemental Material [21] for representation analysis). The determined magnetic structure, shown on Fig. 13, is an amplitude modulated transverse spin structure where the spins are mainly collinearly aligned in the (a, c) plane perpendicularly to the propagation direction b. However, the refinement of a small component along the b axis significantly improves the fit, and the proposed magnetic model is not purely collinear. The ordered magnetic moment is of 8.6(4) μ_B/Ho, which is very close to the value found from powder neutron diffraction measurements [28]. At $T = 4.5$ K and $\mu_0 H = 0$ T, the same magnetic structure model gives satisfactory results with a refined magnetic moment of 7.5(2) μ_B/Ho (Table S8 in the Supplemental Material [21]).

The application of a magnetic field along the a axis causes a lock-in of the propagation vector to a commensurate $k_{2/3} = (0, \frac{2}{3}, 0)$ value, as shown on Figs. S5(a) and S5(b) in the Supplemental Material [21], corresponding to phase II in Fig. 7. The magnetic structure was first determined at $T = 2$ K and $\mu_0 = 1$ T to reach the first metamagnetic step. There, a clear magnetic signal at k_0 was also measured, in addition to $k_{2/3}$, like the $\frac{1}{3}$ phase (labeled III in Fig. 5) of Dy i-MAX. The k_0 magnetic signal is extracted by subtraction of the intensity of the k_0 reflections recorded at $\mu_0 = 1$ T to the same reflection recorded at zero field. The statistics of the extracted k_0 magnetic signal are therefore worse than the pure magnetic reflections collected at $k_{2/3}$. A ferrimagnetic up-up-down structure fits the data reasonably well and explains adequately the $\frac{1}{3}$ magnetization plateau observed in

the bulk magnetization. The magnetic moments are mainly aligned along the a axis, with small b and c components (Fig. 13). It is worth noting that those b and c components are associated with large uncertainties (see Table S9 in the Supplemental Material [21]). The magnitude of the Ho magnetic moment determined by neutron diffraction is 9.0(3) μ_B, which gives a total magnetization of 3.0(1) μ_B per Ho (details in Table S9 in the Supplemental Material [21]). This is close to the value measured in the bulk magnetization.

At $T = 2$ K and $\mu_0 H = 4$ T, the signal at $k_{2/3} = (0, \frac{2}{3}, 0)$ disappears, and only the k_0 magnetic peaks persist. The magnetic structure determination of the FM phase (denoted III in Fig. 7) is based on a similar consideration as Dy i-MAX. The moments are mostly aligned along the a axis, with b and c axis components (Fig. 13). The b axis component switches in sign at each plane: The AFM coupling along this direction is forced by symmetry. The refined ordered magnetic moment is 5.7(2) μ_B, which is surprisingly small with respect to the bulk magnetization data and the structures at zero field and 1 T. This lack of consistency could be ascribed to the poor quality of the data. As mentioned above, the k_0 signal is extracted through a subtraction, which yields worse statistics than direct measurement. It is also worth noting that the b component is larger than in the up-up-down structure described above, in proportion to the total moment. This is puzzling, as one could expect that a larger field would cant the moments toward the direction of applied field, resulting in an equal or smaller b component. The poor quality of the data could also explain this strange behavior by leading to an overestimation of the b component. A magnetic structure refinement with moments confined along a was attempted but leads to a substantially lower quality factor.

The phase labeled IV in Fig. 7 corresponds to the paramagnetic state.

IV. CONCLUSIONS

Bulk magnetization measurements conducted on Ho and Dy i-MAX single crystals highlight a strongly anisotropic behavior. Magnetization as a function of T shows two transitions on Dy i-MAX and one on Ho i-MAX, which is confirmed by specific heat and resistivity measurements. Magnetization as a function of applied field at temperatures below the transitions reveals a metamagnetic behavior, with multiple steps, and hysteretic transitions in the case of Dy i-MAX. XMCD measurements reveal a weak magnetic polarization of the Mo $4d$ and Al $3p$ states that is induced by hybridization with magnetic electronic states of the RE atoms. A quantitative estimation of the orbital and spin moments of the Mo $4d$ orbital was performed with the help of magneto-optical sum rules and suggests a possible direct interaction between the RE $4f$ and the Mo $4d$ magnetic moments. The neutron diffraction data reveal many similarities between the magnetic structures of Ho and Dy i-MAX. Both compounds feature a zero-field incommensurate modulated moment magnetic structure, turning to commensurability at lower T in the case of Dy i-MAX. The first field-induced transition leads to an up-up-down configuration, explaining the $\frac{1}{3}$ step observed in the bulk magnetization and element-selective magnetization curves recorded with XMCD.

Within the planes, there seems to be a strong AFM coupling between the first neighbors which, given the triangular RE lattice, gives rise to geometrical frustration. This first neighbor frustration persists at the $\frac{1}{3}$ up-up-down step. On the other hand, longer-range interactions along the *a* and *b* axes seem to be FM. The changing nature of the coupling as a function of distance is characteristic of the RKKY interaction, which could also contribute to the magnetic frustration by inducing competing interactions. In the manner of many other RE-based intermetallic families, magnetocrystalline anisotropy and RKKY interaction then seem to be the two main driving forces behind the magnetic behavior of Ho and Dy *i*-MAX. When temperature is varied or when a magnetic field is applied, the ground state evolves to a configuration that minimizes the free energy, which leads to the complicated phase diagrams that we have established here. It is worth noting that the evolution of the Néel temperature along the *i*-MAX family does not follow the de Gennes factor, which can be explained in two ways. First, this could result from the CEF splitting of the ground state, which adds CEF terms to the exchange Hamiltonian and could thus drive the T_N evolution away from de Gennes scaling. An updated scaling considering CEF effects can be computed but requires the determination of CEF coefficients [61]. Secondly, this suggests that other types of interactions could have a considerable influence on their magnetic properties. It has been proposed that RE planes could be coupled by dipolar interactions in the Gd *i*-MAX phase, and this may also be the case here [28]. Given the magnitude of the magnetic moments and the distance between two magnetic moments from neighboring planes, the dipolar coupling energy would be ~1 K. However, we notice that the RE planes separated by Al planes (Fig. 1) are always coupled FM (Figs. 12 and 13). This is not compatible with a fully dipolar coupling, which would couple all the planes antiparallel, and suggests that other magnetic interactions are connecting the planes. Moreover, it cannot be excluded that the incommensurate order stems from Fermi surface nesting, which would then add the morphology of the bands to the parameters influencing the magnetic order.

The work on *i*-MAX phases could greatly benefit from an inelastic neutron scattering study, which would provide insight into the magnetic interactions, as well as into the CEF scheme. However, such an experiment is presently made difficult by the small size of the single crystals. In addition, a coupled ARPES and DFT study could bring to light nesting in the band structure, thus helping to settle the question of the origin of the incommensurate order.

[1] D. Gignoux and D. Schmitt, J. Alloys Compd. **326**, 143 (2001).

[2] D. I. Gorbunov, M. S. Henriques, N. Qureshi, B. Ouladdiaf, C. Salazar Mejía, J. Gronemann, A. V. Andreev, V. Petříček, E. L. Green, and J. Wosnitza, Phys. Rev. Mater. **2**, 084406 (2018).

[3] D. Brunt, G. Balakrishnan, D. A. Mayoh, M. R. Lees, D. Gorbunov, N. Qureshi, and O. A. Petrenko, Sci. Rep. **8**, 232 (2018).

[4] G. Drachuck, A. E. Böhmer, S. L. Bud'ko, and P. C. Canfield, J. Magn. Magn. Mater. **417**, 420 (2016).

[5] Q. Tao, J. Lu, M. Dahlqvist, A. Mockute, S. Calder, A. Petruhins, R. Meshkian, O. Rivin, D. Potashnikov, E. N. Caspi, H. Shaked, A. Hoser, C. Opagiste, R. Galera, R. Salikhov, U. Wiedwald, C. Ritter, A. R. Wildes, B. Johansson, L. Hultman *et al.*, Chem. Mater. **31**, 2476 (2019).

[6] A. Farle, L. Boatemaa, L. Shen, S. Gövert, J. B. W. Kok, M. Bosch, S. Yoshioka, S. van der Zwaag, and W. G. Sloof, Smart Mater. Struct. **25**, 084019 (2016).

[7] E. N. Hoffman, D. W. Vinson, R. L. Sindelar, D. J. Tallman, G. Kohse, and M. W. Barsoum, Nucl. Eng. Des. **244**, 17 (2012).

[8] D. Pinek, T. Ito, M. Ikemoto, K. Yaji, M. Nakatake, S. Shin, and T. Ouisse, Phys. Rev. B **100**, 075144 (2019).

[9] M. Naguib, M. Kurtoglu, V. Presser, J. Lu, J. Niu, M. Heon, L. Hultman, Y. Gogotsi, and M. W. Barsoum, Adv. Mater. **23**, 4248 (2011).

[10] A. Gkountaras, Y. Kim, J. Coraux, V. Bouchiat, S. Lisi, M. W. Barsoum, and T. Ouisse, Small **16**, 1905784 (2020).

[11] T. Ouisse, E. Sarigiannidou, O. Chaix-Pluchery, H. Roussel, B. Doisneau, and D. Chaussende, J. Cryst. Growth **384**, 88 (2013).

[12] L. Shi, T. Ouisse, E. Sarigiannidou, O. Chaix-Pluchery, H. Roussel, D. Chaussende, and B. Hackens, Acta Mater. **83**, 304 (2015).

[13] A. Rogalev and F. Wilhelm, Phys. Met. Metallogr. **116**, 1285 (2015).

[14] L. Joly, E. Otero, F. Choueikani, F. Marteau, L. Chapuis, and P. Ohresser, J. Synchrotron Radiat. **21**, 502 (2014).

[15] P. Ohresser, E. Otero, F. Choueikani, K. Chen, S. Stanescu, F. Deschamps, T. Moreno, F. Polack, B. Lagarde, J. P. Daguerre, F. Marteau, F. Scheurer, L. Joly, J. P. Kappler, B. Muller, O. Bunau, and P. Sainctavit, Rev. Sci. Instrum. **85**, 013106 (2014).

[16] A. S. Wills, Physica B **276**, 680 (2000).

[17] J. Rodriguez-Carvajal, Physica B **192**, 55 (1993).

[18] H. T. Stokes, D. M. Hatch, and B. J. Campbell, ISOTROPY Software Suite, iso.byu.edu.

[19] J. M. Perez-Mato, S. V. V. Gallego, E. S. S. Tasci, L. Elcoro, G. De Flor, M. I. I. Aroyo, G. de la Flor, and M. I. I. Aroyo, Annu. Rev. Mater. Res. **45**, 217 (2015).

[20] V. Petricek, M. Dusek, and L. Palatinus, Z. Kristallogr. **229**, 345 (2014).

[21] See Supplemental Material at http://link.aps.org/supplemental/10.1103/PhysRevB.105.174421 for additional information on data analysis of XMCD and neutron diffraction.

[22] Q. Tao, M. Barbier, A. Mockute, C. Ritter, R. Salikhov, U. Wiedwald, S. Calder, C. Opagiste, R-M. Galera, M. Farle, T. Ouisse, and J. Rosen, J. Phys.: Condens. Matter **34**, 215801 (2022).

[23] H. S. Lee, H. B. Kim, R. E. Kim, and W. C. Lee, J. Korean Phys. Soc. **34**, 88 (1999).

[24] B. K. Cho, B. N. Harmon, D. C. Johnston, and P. C. Canfield, Phys. Rev. B **53**, 2217 (1996).

[25] T. Shigeoka, S. Kawano, N. Iwata, and H. Fujii, Physica B **180-181**, 82 (1992).

[26] D. Gignoux, D. Schmitt, J. Voiron, F. Y. Zhang, E. Bauer, and G. Schaudy, J. Alloys Comp. **191**, 139 (1993).

[27] D. Gignoux, D. Schmitt, A. Takeuchi, F. Y. Zhang, C. Rouchon, and E. Roudaut, J. Magn. Magn. Mater. **98**, 333 (1991).

[28] D. Potashnikov, E. N. Caspi, A. Pesach, Q. Tao, J. Rosen, D. Sheptyakov, H. A. Evans, C. Ritter, Z. Salman, P. Bonfa, T. Ouisse, M. Barbier, O. Rivinc, and A. Keren, Phys. Rev. B **104**, 174440 (2021).

[29] A. Champagne, F. Bourdarot, P. Bourges, P. Piekarz, D. Pinek, I. Gélard, J.-C. Charlier, and T. Ouisse, Mater. Res. Lett. **6**, 378 (2018).

[30] C. Sorg, A. Scherz, K. Baberschke, H. Wende, F. Wilhelm, A. Rogalev, S. Chadov, J. Minár, and H. Ebert, Phys. Rev. B **75**, 064428 (2007).

[31] D. Mitcov, M. Platunov, C. D. Buch, A. Reinholdt, A. R. Døssing, F. Wilhelm, A. Rogalev, and S. Piligkos, Chem. Sci. **11**, 8306 (2020).

[32] J. C. Lang, G. Srajer, C. Detlefs, A. I. Goldman, H. König, X. Wang, B. N. Harmon, and R. W. McCallum, Phys. Rev. Lett. **74**, 4935 (1995).

[33] H. Wende, Z. Li, A. Scherz, G. Ceballos, K. Baberschke, A. Ankudinov, J. J. Rehr, F. Wilhelm, A. Rogalev, D. L. Schlagel, and T. A. Lograsso, J. Appl. Phys. **91**, 7361 (2002).

[34] M. Barbier, F. Wilhelm, D. Pinek, K. Furuta, T. Ito, Y. Kim, M. Magnier, D. Braithwaite, M. Vališka, C. Opagiste, M. W. Barsoum, P. Ohresser, E. Otero, P. Le Fèvre, F. Bertran, G. Garbarino, A. Rogalev, and T. Ouisse, Phys. Rev. B **102**, 155121 (2020).

[35] B. T. Thole, P. Carra, F. Sette, and G. van der Laan, Phys. Rev. Lett. **68**, 1943 (1992).

[36] P. Carra, B. T. Thole, M. Altarelli, and X. Wang, Phys. Rev. Lett. **70**, 694 (1993).

[37] P. Blaha, K. Schwarz, F. Tran, R. Laskowski, G. K. H. Madsen, and L. D. Marks, J. Chem. Phys. **152**, 074101 (2020).

[38] J. P. Perdew, K. Burke, and M. Ernzerhof, Phys. Rev. Lett. **77**, 3865 (1996).

[39] M-A. Arrio, J. Long, C. Cartier dit Moulin, A. Bachschmidt, V. Marvaud, A. Rogalev, C. Mathonière, F. Wilhelm, and P. Sainctavit, J. Phys. Chem. C **114**, 593 (2010).

[40] A. Wawro, E. Milińska, Z. Kurant, A. Pietruczik, J. Kanak, K. Ollefs, F. Wilhelm, A. Rogalev, and A. Maziewski, J. Synchrotron Rad. **25**, 1400 (2018).

[41] M. S. S. Brooks, O. Eriksson, and B. Johansson, J. Phys.: Condens. Matter **1**, 5861 (1989).

[42] I. A. Campbell, J. Phys. F: Metal Phys. **2**, L47 (1972).

[43] F. Wilhelm, P. Poulopoulos, H. Wende, A. Scherz, K. Baberschke, M. Angelakeris, N. K. Flevaris, and A. Rogalev, Phys. Rev. Lett. **87**, 207202 (2001).

[44] V. Kapaklis, P. T. Korelis, B. Hjörvarsson, A. Vlachos, I. Galanakis, P. Poulopoulos, K. Özdoğan, M. Angelakeris, F. Wilhelm, and A. Rogalev, Phys. Rev. B **84**, 024411 (2011).

[45] S. V. Gallego, J. M. Perez-Mato, L. Elcoro, E. S. Tasci, R. M. Hanson, K. Momma, M. I. Aroyo, and G. Madariaga, J. Appl. Cryst. **49**, 1750 (2016).

[46] S. V. Gallego, J. M. Perez-Mato, L. Elcoro, E. S. Tasci, R. M. Hanson, M. I. Aroyo, and G. Madariaga, J. Appl. Cryst. **49**, 1941 (2016).

[47] D. Gignoux and D. Schmitt, Phys. Rev. B **48**, 12682 (1993).

[48] J. Dong, H. J. Zhang, G. Xu, Z. Li, G. Li, W. Z. Hu, D. Wu, G. F. Chen, X. Dai, J. L. Luo, Z. Fang, and N. L. Wang, EPL **83**, 27006 (2008).

[49] J. Van Duijn, J. P. Attfield, and K. Suzuki, Phys. Rev. B **62**, 6410 (2000).

[50] J. W. Lynn, S. Skanthakumar, Q. Huang, S. K. Sinha, Z. Hossain, L. C. Gupta, R. Nagarajan, and C. Godart, Phys. Rev. B **55**, 6584 (1997).

[51] X. Zhu, Y. Cao, J. Zhang, E. W. Plummer, and J. Guo, Proc. Natl Acad. Sci. USA **112**, 2367 (2015).

[52] M. O. Ajeesh, K. Weber, C. Geibel, and M. Nicklas, Phys. Rev. B **102**, 184403 (2020).

[53] G. Wu, H. Chen, T. Wu, Y. L. Xie, Y. J. Yan, R. H. Liu, X. F. Wang, J. J. Ying, and X. H. Chen, J. Phys: Condensed Matter **20**, 422201 (2008).

[54] P. Bourgeois-Hope, S. Y. Li, F. Laliberté, S. Badoux, S. M. Hayden, N. Momono, T. Kurosawa, K. Yamada, H. Takagi, N. Doiron-Leyraud, and L. Taillefer, arXiv:1910.08126.

[55] A. V. Tsvyashchenko, D. A. Salamatin, V. A. Sidorov, A. E. Petrova, L. N. Fomicheva, S. E. Kichanov, A. V. Salamatin, A. Velichkov, D. R. Kozlenko, A. V. Nikolaev, G. K. Ryasny, O. L. Makarova, D. Menzel, and M. Budzynski, Phys. Rev. B **92**, 104426 (2015).

[56] C. Gen-Fu, L. Zheng, L. Gang, H. Wan-Zheng, D. Jing, Z. Jun, Z. Xiao-Dong, Z. Ping, W. Nan-Lin, and L. Jian-Lin, Chin. Phys. Lett. **25**, 3403 (2008).

[57] R. H. Liu, G. Wu, T. Wu, D. F. Fang, H. Chen, S. Y. Li, K. Liu, Y. L. Xie, X. F. Wang, R. L. Yang, L. Ding, C. He, D. L. Feng, and X. H. Chen, Phys. Rev. Lett. **101**, 087001 (2008).

[58] D. Gignoux and D. Schmitt, in *Handbook of Magnetic Materials*, edited by K. H. J. Buschow (Elsevier, Amsterdam, 1997), Vol. 10, p. 239.

[59] D. Gignoux, J. C. Gomez-Sal, R. Lemaire, and A. de Combarieu, Solid State Commun. **21**, 637 (1977).

[60] J. A. Blanco, D. Schmitt, and J. C. Gómez Sal, J. Magn. Magn. Mater. **116**, 128 (1992).

[61] D. T. Adroja and S. K. Malik, Phys. Rev. B **45**, 779 (1992).